

An OPPT for a PMSG with a new SEPIC-BUCK converter for a wind-driven PMSG system used in rural areas

Walid Emar^{1*}, Hani Attar^{1,2}, Omar A. Saraereh³,
Mohammad Qabaja⁴, Osama Fares⁵

¹ Energy Engineering Department, Faculty of Engineering Technology, Zarqa University, Zarqa, 13110, Jordan

² Engineering Department, College of Engineering, University of Business and Technology, Jeddah, 21448, Saudi Arabia

³ Faculty of Engineering, Electrical Engineering Department, The Hashemite University, Zarqa, 13115, Jordan

⁴ Civil Engineering Department, Faculty of Engineering, Zarqa University, Amman, 11622, Jordan

⁵ Electrical Engineering Department, Faculty of Engineering, Isra University, Amman, 11622, Jordan

ABSTRACT

The voltage of a permanent magnet synchronous generator (PMSG) driven directly by a wind turbine is variable due to the intermittent nature of wind energy. Voltage disturbances and power fluctuations are the main problems of PMSG systems based on converters driven by wind turbines. In this paper, the invented double-switch SEPIC-buck (DSSB) converter scheme is eventually used for system optimization to achieve the required OPPT and to keep power transfer at the highest efficiency when the load parameters characteristics (current and voltage) are changed. A DSSB converter small signal technique is used in the simulation/control process to analyze and simulate the small signal deviation from the steady-state operating point of the converter input parameters (voltage and current). This helps to determine the small deviation of the converter duty cycle and thus the small AC signals of the converter output voltage and load current as input control parameters. The small-signal principle is authorized by taking into consideration the DSSB converter to serve as a linear time-invariant system centered on OPPT as the point of operation with importance. Thanks to the small signal analysis with the current control scheme, wherein the condition of the overcurrent, the DSSB is classified as safe.

Keywords: Wind turbine (WT), Permanent-magnet synchronous generator (PMSG), Small-signal analysis, Current-mode control.

OPEN ACCESS

Received: August 10, 2023
Revised: October 23, 2023
Accepted: December 18, 2023

Corresponding Author:

Walid Emar
Wemar@zu.edu.jo

 **Copyright:** The Author(s). This is an open access article distributed under the terms of the [Creative Commons Attribution License \(CC BY 4.0\)](https://creativecommons.org/licenses/by/4.0/), which permits unrestricted distribution provided the original author and source are cited.

Publisher:

[Chaoyang University of Technology](https://www.chaoyang.edu.cn/)

ISSN: 1727-2394 (Print)

ISSN: 1727-7841 (Online)

1. INTRODUCTION

Energy production from wind has become essential in providing low-cost electricity in isolated rural areas and has become a very fast-growing renewable energy source of world energy consumption. Grid-connected renewable energy systems are often unavailable, so auxiliary power electronic systems for stand-alone self-operation are developed to meet this need (Emar et al., 2019; Adhul et al., 2020).

The increasing integration of wind turbines (WTs) has aroused interest in calculating and investigating the required power of synchronous generators to supply isolated loads (Emar, 2016; Boufadene et al., 2018; Emar et al., 2019). The rapid development of medium and low-power WTs and the development of new technologies contributed to

the intensive development of independent WECS (Yazdani, 2010; Emar et al., 2011; Azzaoui et al., 2017; Emar, 2024).

All electrical machines depend on the induction of a magnetic field for energy conversion. Due to several advantages, the synchronous generator is traditionally preferred over other electrical machines for use in power generation in stand-alone plants. Some of them are a cooling system that provides excellent cooling performance, is highly suitable for hot and tropical climates, high availability, higher energy production due to permanent magnet excitation, lower maintenance costs, and reduced noise level due to fewer moving parts (Boufadene, 2018).

The wind energy conversion system produces the optimal power point tracking (OPPT) by utilizing variable-speed wind energy conversion systems (WECS) and a three-phase permanent magnet synchronous generator (PMSG) with a new high-gain DC-DC converter scheme called a double-switch SEPIC-buck converter (DSSB). Usually, PMSGs with power electronic converters are widely used, especially in low/medium power applications of WECS. Their ability to maintain full torque at low speeds and less heat generation in the rotor circuit with low torque ripple provides high efficiency and high power density (Emar et al., 2011; Emar, 2016; Azzaoui et al., 2017).

WECS have varying relationships to power electronic processors, AC networks, and other electrical loads. The main problem solved by power point tracking is that the efficiency of power transmission in these systems is not fixed and changes with the wind speed (Emar et al., 2020).

A power curve in Fig. 1 shows how the power and thereby, the electricity generated by the WT can vary within two limits of wind speed, cut-in, and out speeds. When the wind exceeds the tripping speed, the power increases significantly. However, at certain speeds, called rated wind speed, the power reaches a level, called rated power, at which the electric generator can continue to operate. This is the maximum level (optimum speed and optimum power) that the electrical generator can still work. As soon as the wind speed becomes higher than the cut-out speed, the power is kept almost constant by using, for instance, the pitch system for controlling the blade angles (Bosco et al., 2014; Azzaoui et al., 2017; Boufadene et al., 2018).

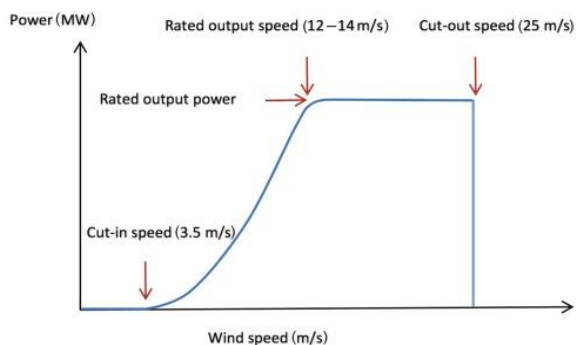


Fig. 1. A typical operating region and power curve for a WT

Thus, when the condition of the atmosphere is changed, the load resistance that produces the highest power transfer and efficiency also changes. The system then needs to be optimized when the load impedance changes to keep power transfer at the highest efficiency. This optimum load impedance may be called the OPPT. Hence, OPPT is the algorithmic way of adjusting the load impedance for extracting the maximum available power from WECS as the operating conditions change. The voltage at which an electrical generator-based WT can produce maximum power is called OPPT. Power electronic converters can be designed to present optimum load characteristics to the WECS and then regulate the voltage, current, and frequency to suit the required power transfer and efficiency.

As a remedy for this problem, a new OPPT converter with a suitable algorithm is explored in this paper. A diode rectifier followed by a new scheme of DSSB essentially used for the interfacing of the WECS with PMSG supplying a DC load, DC motor drive, or DC transmission line, and a proposed control strategy for a standalone system is presented. The proposed configuration of the "WECS" wind energy conversion system is shown in Fig. 2. There are many possible converter topologies and converter switching schemes, and each can have its relative advantages and disadvantages (Magossi et al., 2020).

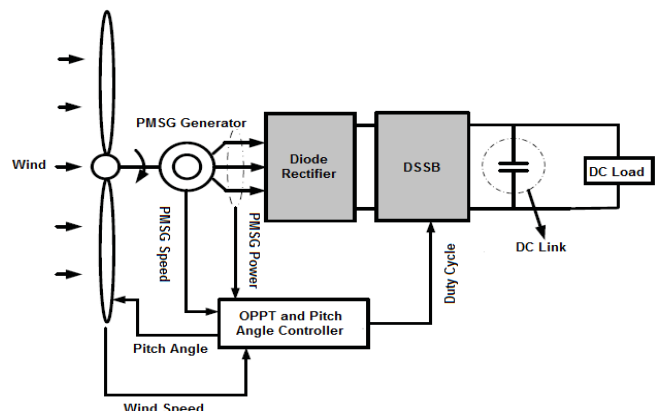


Fig. 2. Stand-alone WECS with a PMSG connected to a dc power grid, DC transmission lines, or DC load through a DSSB converter with a DC link and rectifier circuit

Thus, a new DSSB for WECS with PMSG that allows users to use electric generators with a higher voltage output than the operating voltage of WECS is proposed. DSSB is a DSSB that works in both regimes, bucking, and boosting and provides higher voltage gain than other conventional DC-DC converters (Buck, SEPIC, Boost, and Buck-Boost) and better dynamic properties (Emar et al., 2019; Jiang et al., 2020; Emar et al., 2024).

The proposed OPPT approach is related to the ideal tip speed ratio and the ideal PMSG torque control. The method allows for the greatest amount of generated turbine power to be achieved by controlling the PMSG torque and tip speed ratio while monitoring the wind speed with a wind

speed sensor. Utilizing the recorded wind speed, the reference optimal speed ω_{opt} of the PMSG is determined. This speed is used to compute the turbine torque and power. The rated specifications of the PMSG and the WT can be used to compute the coefficient of optimal power k_{opt} (El-Hasan et al., 2000; Gajewski et al., 2023).

The gating signals for the voltage source inverter (VSI) are created based on the control of PMSG stator currents and voltages. The control algorithm used with the proposed DSSB converter operates by repeatedly examining the rate of change in power in comparison to the rate of change in generator stator voltage. The DSSB DC-DC converter is designed to transfer power and voltage to the load efficiently while fabricating the minimum rate of current and voltage ripple possible at the input and output. In this case, the constant rate of input power change in response to the change in generator stator voltage is controlled by two PI current-mode controllers. After choosing the appropriate gain value of the two PI controllers using the trial-and-error method, the AC small signal analysis using the PI controllers is utilized to develop the best switching methodology for the DSSB switches (Mostaan et al., 2017; Emar et al., 2024).

Utilizing Simulink and Simplorer, the converter was simulated, and the results were in line with the output voltage gain determined by analysis for a strictly resistive load. With a voltage gain of $(D(1+D))/(1-D)$, the suggested converter achieves a peak efficiency of 96%–98%. The AC small signal method and PI current controllers were used to examine the stability and dynamic response of the recommended converter with the system of WECS. The findings show the converter has a good performance in conditions of the time for low rise, settling, and overshoot, gain margin, and the phase margin with 0.05 s, 0.2 s, 82 dB at 1 e4 rad/s , and 45 degrees at 700 rad/s, respectively.

This OPPT DSSB converter can be used with other renewable energy sources such as offshore turbines, PV solar cells, etc. The power at the OPPT converter output/input is the product of the OPPT converter output/input voltage and current.

The remaining sections of the paper are structured as follows: section II is dedicated to the physical description and construction of the PMSG, section III represents the mechanical and WT model, section IV is about the DSSB converter, section V discusses the control strategy for the PMSG-based wind energy conversion inverter system, section VI discusses the results of simulations and experiments, and section VII discusses the research's conclusions.

2. PMSG CONSTRUCTION AND PHYSICAL DESCRIPTION

The PMSG contains two essential parts, the first one is the rotating part (rotor) and the second part is stationary (stator). The supply voltage is essentially generated in the

armature winding, which is mounted on the stator. However, the main magnetic flux is produced by a permanent magnet located within the rotor circuit.

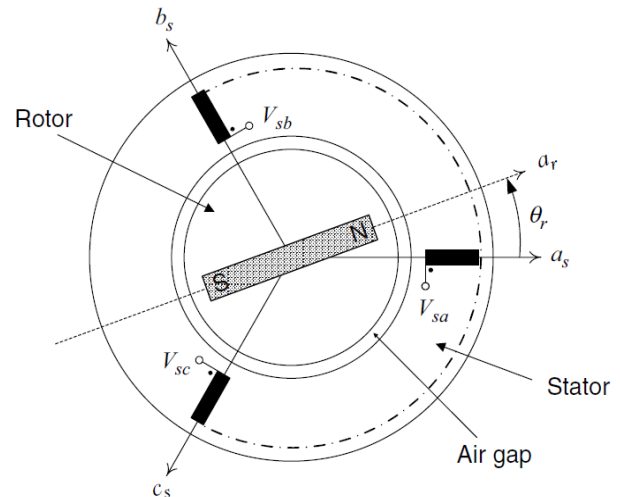


Fig. 3. Simplified schematic of a three-phase PMSG

Fig. 3 shows a cross-section of a three-phase PMSG. The three windings of the armature circuit are displaced 120° relative to each other and produce three-phase voltages, v_{sa} , v_{sb} , and v_{sc} that present sinusoidal waveforms at the input terminals (Yazdani et al., 2010; Magossi et al., 2020; Guesmi et al., 2021).

Essentially, the working principle of the synchronous generator relies on the following equation:

$$n = 120f/p \tag{1}$$

Where f is the supply frequency and p pole-pair of the machine.

2.1 Three-phase Model

To model the PMSG, it is assumed that there is no damping winding in the rotor. Moreover, the rotor saliency is neglected which means that PMSG has a uniform air gap. If the currents flowing into the stator three-phase windings, i_{sa} , i_{sb} , i_{sc} form a balanced three-phase set, then the magnetic flux linkage equations with each of the coils sa , sb , sc , and the permanent magnet are created due to its current and the currents in the remaining coils. Thus, after the substitution, the flux coupling equations for each stator and rotor current for the three coils are written as:

$$\begin{bmatrix} \lambda_{sa} \\ \lambda_{sb} \\ \lambda_{sc} \end{bmatrix} = \begin{bmatrix} L_s & M_s & M_s \\ M_s & L_s & M_s \\ M_s & M_s & L_s \end{bmatrix} \begin{bmatrix} i_{sa} \\ i_{sb} \\ i_{sc} \end{bmatrix} + \begin{bmatrix} \lambda_{ar} \\ \lambda_{br} \\ \lambda_{cr} \end{bmatrix} \tag{2}$$

Where M_s is the mutual inductance between each adjacent pair of stator coils, and L_s is the self-inductance of these coils. The mutual fluxes (λ_{ar} , λ_{br} , λ_{cr}) between the permanent magnet of the rotor and each stator coil varies

with the position of the rotor in a cosine-like manner.

Therefore, if the rotor is assumed to rotate at a constant angular speed ω_r , then the speed and position of the rotor of the two-pole generator change as follows:

$$\omega_r = \frac{d\theta_r}{dt} \Rightarrow \theta_r = \omega_r t + \theta_o \quad (3)$$

Where θ_r represents the rotor permanent magnet position concerning the reference coil of the stator, sa, and θ_o is the angle between the rotor axis and coil sa at $t = 0$. After substituting for the rotor flux, the expressions for the fluxes linked by the stator take on the following simpler form:

$$\begin{aligned} \lambda_{sa} &= (L_s + M_s) i_{sa} + \lambda_{rm} \cos(\omega_r t + \theta_o) \\ \lambda_{sb} &= (L_s + M_s) i_{sb} + \lambda_{rm} \cos(\omega_r t + \theta_o - 120^\circ) \\ \lambda_{sc} &= (L_s + M_s) i_{sc} + \lambda_{rm} \cos(\omega_r t + \theta_o + 120^\circ) \end{aligned} \quad (4)$$

The generator mode convention is used in this thesis since wind energy is the case study. As a result, the stator current's direction is chosen to be positive, as shown in Equation (4) (Oner et al., 2010). Each one of these three equations has two flux mutual components - one due to the rotor fluxes ($\lambda_{ar} = \lambda_{rm} \cos(\omega_r t + \theta_o)$, $\lambda_{br} = \lambda_{rm} \cos(\omega_r t + \theta_o - 120^\circ)$, $\lambda_{cr} = \lambda_{rm} \cos(\omega_r t + \theta_o + 120^\circ)$), and the other due to the stator (armature) currents (i_{sa} , i_{sb} , i_{sc}). If each coil (phase) has a resistance R_s and synchronous reactance $X_s = \omega_s (L_s + M_s)$, as shown in Fig. 4, then the voltage drop across each phase is given as:

$$\begin{aligned} v_{sa} &= -R_s i_{sa} - (L_s + M_s) \frac{di_{sa}}{dt} + \sqrt{2} E_m \sin(\omega_r t + \delta + 90^\circ) \\ v_{sb} &= -R_s i_{sb} - (L_s + M_s) \frac{di_{sb}}{dt} + \sqrt{2} E_m \sin(\omega_r t + \delta - 30^\circ) \\ v_{sc} &= -R_s i_{sc} - (L_s + M_s) \frac{di_{sc}}{dt} + \sqrt{2} E_m \sin(\omega_r t + \delta + 210^\circ) \end{aligned} \quad (5)$$

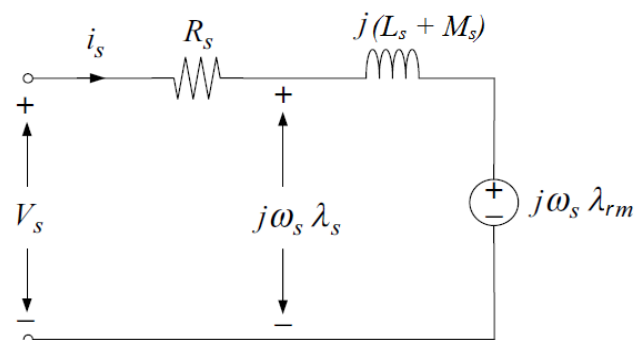


Fig. 4. Phasor-domain (steady-state) equivalent circuit of the PMSG

The negative signs are applied for the generation action of the machine. The angle $\delta = \theta_o - 90^\circ$ indicates the position of the q-axis which is behind the direct axis (d) by 90° . The effect of the permanent magnet on the stator coils appears in the form of the machine-generated (synchronous, internal)

voltage, which is $e_{sa} = \sqrt{2} E_m \sin(\omega_r t + \delta + 90^\circ)$ for coil sa (Ali et al., 2013; Magossi et al., 2020).

In Fig. 4 a stationary equivalent circuit for a PMSG is developed, where it is assumed that the rotor shaft speed is equal to the stator voltage of angular frequency.

2.2 Two-phase Model

The main objective of the two-phase model (dq-model) shown in Fig. 5 is to eliminate the dependence of inductors on the position of the rotor. The dq transformation may be represented as visualizing a fictitious PMSG with orthogonal stator axes that are fixed magnetically to the rotor dq-axes. Thus:

$$\begin{aligned} v_{ds} &= -R_s i_{ds} - \frac{d\lambda_{ds}}{dt} + \omega_r \lambda_{qs} \\ v_{qs} &= -R_s i_{qs} - \frac{d\lambda_{qs}}{dt} + \omega_r \lambda_{ds} \end{aligned} \quad (6)$$

The zero-sequence component of the above stator voltages and currents has zero value due to the balanced condition of the proposed system. Based on Equation (7), and under the dynamic behavior of a sinusoidally distributed winding and a constant air gap, it can be assumed that:

$$\begin{aligned} v_{qs} &= -R_s i_{qs} - L_{qs} \frac{di_{qs}}{dt} + \omega_r (L_{ds} i_{ds} + \lambda_{rm}) \\ v_{ds} &= -R_s i_{ds} - L_{ds} \frac{di_{ds}}{dt} + \omega_r (L_{qs} i_{qs}) \end{aligned} \quad (7)$$

Relatively elegant expressions for the (d) and (q) axis inductors L_{ds} and L_{qs} , respectively, are obtained as follows:

$$\begin{aligned} L_{ds} &= L_{ls} + L_{dm} \\ L_{qs} &= L_{ls} + L_{qm} \end{aligned} \quad (8)$$

The so-called cyclic magnetization inductances of synchronous machines L_{dm} and L_{qm} , are proportional to their flux density fundamentals and are estimated in detail (Magossi et al., 2020). Under the condition of their symmetry, the leakage flux inductance L_{ls} is the same for all three phases of the machine (Oner et al., 2010). Thus:

$$\begin{aligned} \lambda_{qs} &= (L_{ls} + L_{qm}) i_{qs} \\ \lambda_{ds} &= (L_{ls} + L_{dm}) i_{ds} + \lambda_{rm} \end{aligned} \quad (9)$$

The equality between the three-phase PMSG and its dq-model in terms of torque, power, and losses is indicated by the coefficient of 2/3 in the Park transformation. Thus:

$$\begin{aligned} V_{sa} I_a + V_{sb} I_b + V_{sc} I_c &= \frac{3}{2} (V_{ds} I_{ds} + V_{qs} I_{qs}) \\ T_{em} &= \frac{3}{2} p (\lambda_{ds} i_{qs} - \lambda_{qs} i_{ds}) \\ R_s (i_{sa}^2 + i_{sb}^2 + i_{sc}^2) &= \frac{3}{2} R_s (i_{ds}^2 + i_{qs}^2) \end{aligned} \quad (10)$$

After substituting for λ_{ds} and λ_{qs} in Equation (10), one may get the following equation for the machine torque:

$$T_{em} = \frac{3}{2} (L_{ds} - L_{qs}) i_{qs} i_{ds} + \frac{3}{2} \lambda_{rm} i_{qs} \quad (11)$$

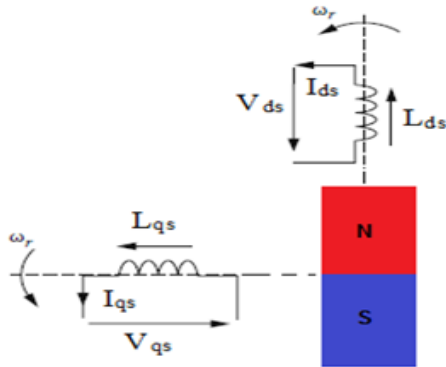


Fig. 5. The dq model of PMSG

Again, L_d and L_q are the dq-axis stator circuit inductances that are associated with rotor saliency and machine geometry. In this paper, the rotor is non-salient, with non-significant saliency; therefore, $L_{ds} = L_{qs}$. Thus, the product component $i_{ds} \times i_{qs}$ does not contribute significantly to T_e . Therefore, in this case, i_{sd} can be regulated to have a zero value to minimize the losses. The machine torque is therefore given as a function of only the current i_{qs} :

$$T_{em} = \frac{3}{2} \lambda_{rm} i_{qs} \quad (12)$$

The parameter λ_{rm} represents the maximum constant flux value generated by the rotor permanent magnet and shared by the stator windings. The PMSG of power active and reactive is expressed as follows:

$$\begin{aligned} P_{gen} &= \frac{3}{2} [V_{sq} I_{sq} + V_{sd} I_{sd}] = \frac{3}{2} V_{sq} I_{sq} \\ Q_{gen} &= \frac{3}{2} [V_{sq} I_{sd} - V_{sd} I_{sq}] = -\frac{3}{2} V_{sd} I_{sq} \end{aligned} \quad (13)$$

2.3 PMSG Torque Control in Rotor Field Coordinates

To control i_{sd} and i_{sq} , the phase equations of the PMSG are transformed into state space form, and λ_{ds} with λ_{qs} between the two equations are eliminated as follows:

$$\begin{aligned} V_{ds} + \omega_r L_{qs} i_{qs} &= u_d \Rightarrow u_d = R_s i_{ds} + L_{ds} \frac{di_{ds}}{dt} \\ V_{qs} - L_{ds} \omega_r i_{ds} &= u_q \Rightarrow u_q = R_s i_{qs} + L_{qs} \frac{di_{qs}}{dt} + \omega_r \lambda_{rm} \end{aligned} \quad (14)$$

For bipolar (two-pole) permanent synchronous generators, $\omega_r = \omega_s$ applies. i_{ds} and i_{qs} can be set to the required values via two independent current loops with two controlled variables, u_d and u_q , as shown in Fig. 6. Thus, the first compensator with gain $k_d(s)$ is used for current regulation. i_{ds} to the required value and a compensator with a gain of $k_q(s)$ is used to regulate the current i_{qs} . For this reason:

$$\begin{aligned} k_d(s) &= \frac{sL_{ds} + R_s}{s\tau_i} \\ k_q(s) &= \frac{sL_{qs} + R_s}{s\tau_i} \end{aligned} \quad (15)$$

V_{ds} and V_{qs} are determined, respectively, based on Equation (14), and then divided by $V_{dc/2}$ to achieve the switching signals implementation for the inverter as required. The voltage $V_{dc/2}$ is generated at the output of DSSB based on the control technique applied for it.

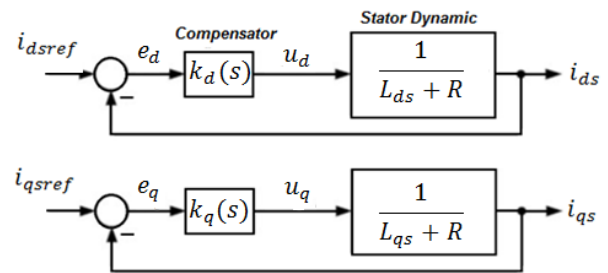


Fig. 6. Block diagrams of the stator current closed loops, based on Equation (13)

3. MECHANICAL AND WIND TURBINE MODEL

The operation of a WT can be represented by its mechanical power specified in (Wu et al., 2018; Emar et al., 2020; Osmani et al., 2021; Masmoudi et al., 2022; Nizami et al., 2022):

$$P_{tur} = \frac{1}{2} \rho A v^3 C_p(\lambda, \beta) \quad (16)$$

A is considered to be the area swept through the turbine, v is the average value of the wind speed throughout interest, ρ is the wind density, and C_p is the limit of Betz or power factor. β is the angle of blade inclination in degrees and λ is a dimensionless ratio between the peripheral speed and the number of revolutions, respectively (Emar et al., 2024).

Thus, Equation (16) indicates that turbine efficiency for a particular turbine depends on two components. The first, $\frac{1}{2} \rho A v^3$, is directly proportional to the wind speed repeated three times, and the second, $C_p(\lambda, \beta)$, is a quantity variable. The first term is invariant because the wind speed is uncontrolled. However, $C_p(\lambda, \beta)$ can be controlled by modifying λ and/or β . Therefore, λ is a function of R/v , where R is the radius of the blade and ω_r is the rotor angular velocity. Control of λ can be achieved by adjusting ω_r and/or β (Nizami et al., 2022).

The output torque of a WT can be expressed as:

$$T_{tur} = \frac{1}{2} \frac{\rho AR v^2 C_p(\lambda, \beta)}{\lambda} \quad (17)$$

Assuming constant swept area, air density, and wind speed, the power delivered from the turbine is determined by the

coefficient of performance (C_p). Therefore, C_p is a function of the ratio between the (λ) maximum speed and the (β) pitch angle, expressed in degrees. So, if β equals zero, in which case C_p is simply a function of λ , then:

$$C_p(\lambda, \beta) = \left(\frac{60.04}{\lambda} - 4.69\right) e^{\left(\frac{-21}{\lambda} + 0.735\right)} + \frac{0.0068\lambda}{1 - 0.035\lambda} \quad (18)$$

The graph of dependence of C_p on the tip speed ratio for different values of blade angle of pitch β is shown in Fig. 7. The optimum tip speed ratio for a three-blade turbine is $\lambda_{max} \cong 8.1$ and the optimum value of C_p is $C_{pmax} \cong 0.48$. However, the optimal power consumption for a WT can be achieved when the turbine operates with optimal C_p (k_{opt}). It is therefore necessary to adjust the rotor speed to the optimum value of the relationship between the maximum speed (λ_{opt}) and the wind speed fluctuations.

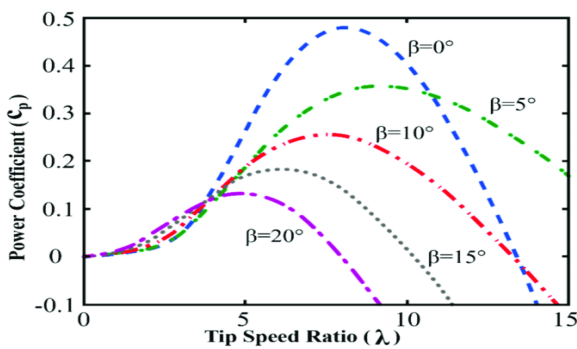


Fig. 7. Power coefficient versus tip-speed ratio for different pitch angles (Nizami et al., 2022)

To achieve the optimum tip speed ratio for optimum power output for three-blade WTs, the formula for (λ_{opt}) has been empirically proven (Wu et al., 2018) as:

$$\lambda_{opt} \approx \frac{4\pi}{3} (1.25) \cong 5.25 \quad (19)$$

Remember that if the rotor spins too slowly, a high of wind will blow between gaps through the blades instead of leading the turbine. But if the blades rotate fast, they can create too much disorder in the air or act as a solid wall against the wind. Therefore, to increase the efficiency of the turbine without subjecting its blades to damage, the optimum speed ratio should be calculated according to Equation (19).

3.1 Control Strategy for Optimal Power-point Tracking (OPPT)

If the speed of wind exceeds a certain rated value, the angle of pitch is increased using a feedback mechanism to limit the turbine/machine output. The pitch of the turbine blades is set to zero at rated power using the pitch control scheme. Therefore, to get optimal performance point tracking, λ is adjusted to λ_{opt} such that $C_p(\lambda, \beta = 0) = C_{opt}$, that is

$C_{opt} = C_p(\lambda_{opt})$. Therefore, after replacing the swept area A of the WT, the optimum power output is given by:

$$P_{opt} = T_{opt} \omega_r = \frac{1}{2} \frac{\rho \pi R^5 C_{opt} \omega_r^3 e f}{\lambda_{opt}^3} = k_{opt} \omega_{ref}^3 \quad (20)$$

And the optimal torque is then given as (Jiang et al., 2020):

$$T_{opt} = \frac{1}{2} \frac{\rho \pi R^5 C_{opt} \omega_r^2}{\lambda_{opt}^3} = k_{opt} v^2 \quad (21)$$

Thus, the constant k_{opt} representing the WT characteristics is (Jiang et al., 2020):

$$k_{opt} = \frac{1}{2} \frac{\rho \pi R^5 C_{opt}}{\lambda_{opt}^3} \quad (22)$$

Equation (21) shows that the turbine torque should be proportional to the square of the optimal turbine speed in a variable speed system with constant λ_{opt} . Therefore, to find the optimum power point without damaging the turbine blades, The algorithm has to make the turbine torque change in proportion to the square of the optimal rotor speed and make sure that the relationship between the turbine speed and the rotor speed is such that $\lambda = \lambda_{opt}$. As Fig. 8 shows, The intersection point of both curves corresponds to the optimal power corresponding to the given wind speed.

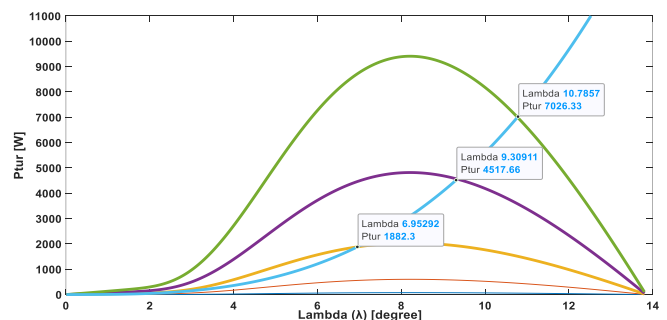


Fig. 8. A plot of an optimal power point tracking strategy based on Equations (20) and (21)

To achieve this optimum, the machine's electromagnetic torque, T_{em} , and ω_{ref} must be regulated and calculated through the OPPT technique and then applied to the PMSG to run the generator at its optimum speed by regulating the WT speed for any wind speed below the rated value. Its expression becomes as indicated by Equation (23).

In addition, the control of pitch angle is also adapted to maintain the WT output power at its rated value. Fig. 9 explains the OPPT implementation technique and Fig. 10 illustrates the control of the pitch angle block diagram.

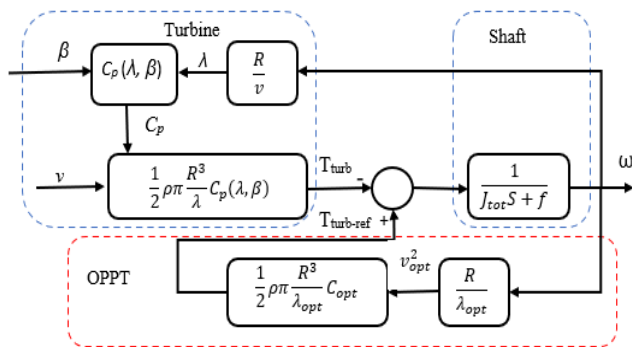


Fig. 9. OPPT implementation technique

Therefore, mechanical pitch control is commonly used to adjust the pitch of the turbine blades according to wind speed to ensure system performance and power at the rated value. This method limits the power output and speed when the generator exceeds 30% of its rated speed (Kanimozhi et al., 2017; Osmani et al., 2021; Nizami et al., 2022).

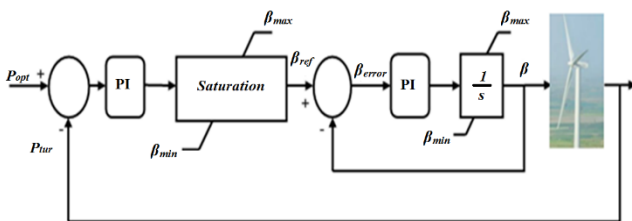


Fig. 10. Pitch angle control block diagram

4. DSSB CONVERTER

It was able to build the DSSB known as the new high-gain DC-DC converter scheme after applying some modifications to the existing recognized SEPIC converter in compliance with accepted processes. The DSSB contains a larger voltage gain and superior dynamic characteristics when compared to other standard DC-DC converters such as (Buck, SEPIC, Boost, and Buck-Boost). A duty cycle is generated by the DSSB converter as part of an OPPT control scheme depending on the available wind speed. As soon as the wind speed surpasses its nominal value, the pitch angle starts. The pitch angle command controls are used to change the turbine blade angle so that the shaft rotational speed is maintained at its ideal level.

Fig. 11 shows the new modified DSSB with the basic structure of it. DSSB may contain a (solar cell system) DC source, an input smoothing inductor L1, a (MOSFET, IGBT, BJT) power electronic switches BJT1 and BJT2, a (Cs, Cm, C1, and Co) capacitive filters, a (Dm1, Dm2, and Dm3) three freewheeling diodes, an (L1, L2, and L3) three smoothing inductors, and lastly the DC resistive load, R.

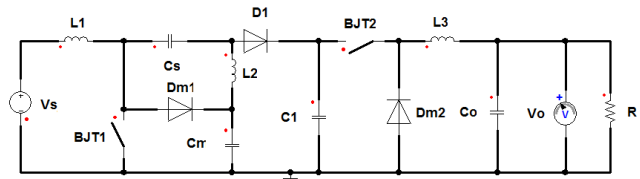


Fig. 11. DSSB converter

4.1 Working Principle of the DSSB

The DC-DC converter is inductor voltages that zero values on the average back on volt-second area balancing principle with the continuous current inductor. Also, other findings show the capacitor voltages exhibit nearly smooth DC and continuous waveforms with the value of zero average for capacitors under steady-state conditions. Table 1 shows the regulator running simulation parameters in (UCCM) uninterrupted conduction current mode:

Table 1. Simulation parameters of DSSB

Parameter and symbol	Real value
Smoothing inductors (L)	10 mH
Solar cell supply voltage (Vs)	50 V
Load resistance (R)	10 Ω
The capacitance of all capacitors (C)	1 mF
Switching frequency (F)	4 kHz

4.2 Bucking and Boosting Regime of the DSSB

The following circuit schematics for the region $0 \leq D \leq 1/2$ help to better comprehend the DSSB operating principle:

Based on Figs. 12, 13, 14 and 15, DSSB is operating in four phases:

The initial phase during the interval $[0, DT]$ is shown in Fig. 12. During this interval, BJT1 is on. The following equations were used to achieve the voltage conversion ratio by using the inductor currents as state variables:

$$\begin{aligned}
 v_{L1} &= L_1 \frac{di_1}{dt} = V_s \\
 v_{L2} &= L_2 \frac{di_2}{dt} = -v_{Cs} - v_{Cm} \\
 v_{L3} &= L_3 \frac{di_3}{dt} = -V_o
 \end{aligned}
 \tag{23}$$

The second phase during the interval $[DT, T/2]$ is shown in Fig. 13. When this interval, BJT1 and BJT2 are off. The outcomes equations describing this phase are:

$$\begin{aligned}
 v_{L1} &= L_1 \frac{di_1}{dt} = V_s - v_{Cm} \\
 v_{L2} &= L_2 \frac{di_2}{dt} = -v_{Cs} = v_{C1} - v_{Cm} \\
 v_{L3} &= L_3 \frac{di_3}{dt} = -V_o
 \end{aligned}
 \tag{24}$$

The third phase, during the interval for $[T/2, T/2 + DT]$ is shown in Fig. 14. During this interval, for BJT1 is off and BJT2 is on. The resulting equations describing this phase are:

$$\begin{aligned}
 v_{L1} &= L_1 \frac{di_1}{dt} = V_s - v_{Cm} \\
 v_{L2} &= L_2 \frac{di_2}{dt} = -v_{Cs} = v_{C1} - v_{Cm} \\
 v_{L3} &= L_3 \frac{di_3}{dt} = v_{C1} - V_o
 \end{aligned}
 \tag{25}$$

The fourth phase is shown again in Fig. 13 during the interval $[T/2 + DT, T]$. During this interval, BJT1 and BJT2 are off. The following equations can be written for this phase:

$$\begin{aligned}
 v_{L1} &= L_1 \frac{di_1}{dt} = V_s - v_{Cm} \\
 v_{L2} &= L_2 \frac{di_2}{dt} = -v_{Cs} = v_{C1} - v_{Cm} \\
 v_{L3} &= L_3 \frac{di_3}{dt} = -V_o
 \end{aligned}
 \tag{26}$$

The following set of equations can be obtained by applying Kirchhoff voltage law to the steady-state mean values of the inductor voltages during various operation phases:

$$\begin{aligned}
 V_{L1} &= V_s - (1 - D) V_{Cm} \\
 V_{L2} &= (1 - D)V_{C1} - DV_{Cs} - V_{Cm} \\
 V_{L3} &= -V_o + D V_{C1} \\
 V_{Cs} &= V_{Cm} - V_{C1}
 \end{aligned}
 \tag{27}$$

According to the volt-seconds area balance where the voltages across the inductors have zero mean values it will derive the following relationships for the capacitive voltages:

$$\begin{aligned}
 V_{Cm} &= \frac{1}{1-D} V_s \\
 V_{Cs} &= -DV_{Cm} = \frac{-D}{1-D} V_s \\
 V_{C1} &= \frac{V_o}{D}
 \end{aligned}
 \tag{28}$$

The following expression for the (V_o) output voltage conversion concerning the (V_s) supply voltage in the range of $0 \leq D \leq 1/2$ will be produced after rearranging the variables:

$$V_o = \frac{D(1+D)}{(1-D)} V_s \tag{29}$$

The maximum value is reached when $V_o = V_s$. when the voltage gain characteristics in the bucking regime of DSSB. Thus:

$$\frac{V_o}{V_s} = \frac{D(1+D)}{(1-D)} = 1 \Rightarrow D = -1 + \sqrt{2} \tag{30}$$

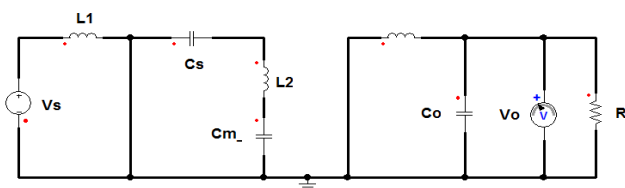


Fig. 12. ON-STATE of BJT1 and OFF-STATE of BJT2 for the region of $0 < D < 1/2$

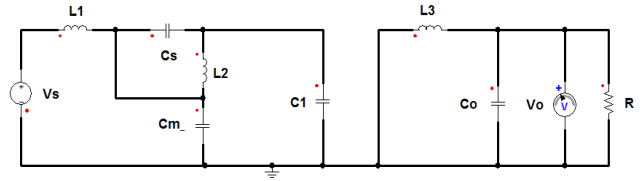


Fig. 13. OFF-STATE of BJT1 and BJT2 for the region of $0 < D < 1/2$

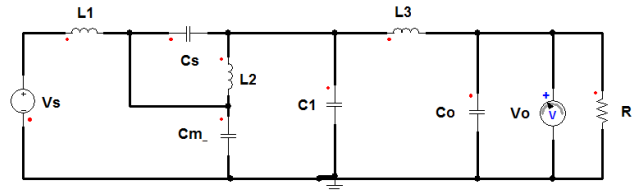


Fig. 14. OFF-STATE of BJT1 and ON-STATE of BJT2 for the region of $0 < D < 1/2$

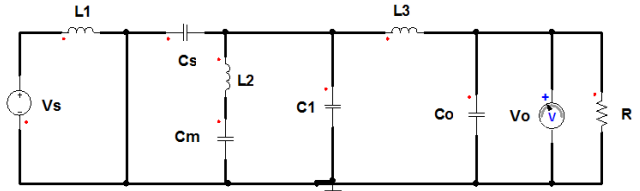


Fig. 15. ON-STATE of BJT1 and BJT2

DSSB combines the capabilities of the buck and boost converters when $(0 < D < -1 + \sqrt{2})$ output voltage magnitude in the bucking regime is less than that of the supply or otherwise greater than the supply. The voltage/current simulation waveforms developed in Matlab/Simulink are shown in Fig. 16 for $D = 0.3$. The DSSB's target switching frequency is $f = 4 \text{ kHz}$. The results indicate that the suggested converter has an efficiency of 96%–98% with a low rise time of 0.1 s and a settling time of 0.2 s.

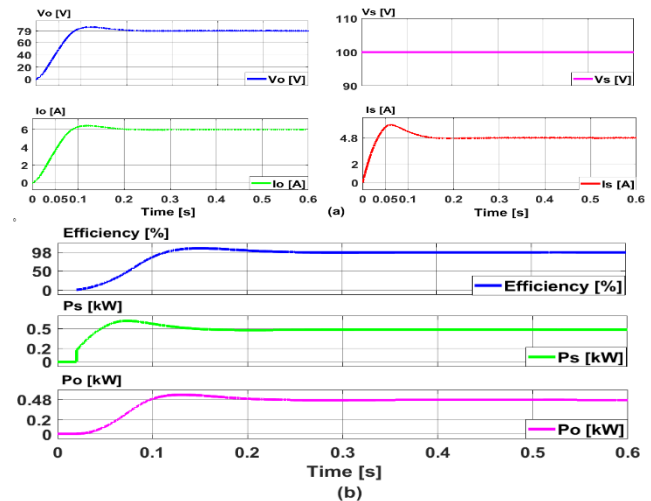


Fig. 16. DSSB voltage and current waveforms in the bucking regime

In the vicinity of $-1 + \sqrt{2} < D < 1$, the second potential operational region of the DSSB is located. Since the gain voltage able only be greater than unity in this region, the converter is in a boosting mode of operation. Within this region, BJT1 and BJT2 changeover timings could coincide. As a result, based on the following figures, One may obtain the different phases of the process for the DSSB under the supposition of the best steady-state operating circumstances for DSSB.

Fig. 15 depicts the initial phase $[0, (2D-1) T]$, during which both BJT1 and BJT2 are active. The following equations can be used by using the inductor currents as state variables, it can obtain an expression for the voltage conversion ratio:

$$\begin{aligned} v_{L1} &= L_1 \frac{di_1}{dt} = V_s \\ v_{L2} &= L_2 \frac{di_2}{dt} = -v_{Cs} - v_{Cm} \\ v_{L3} &= L_3 \frac{di_3}{dt} = v_{C1} - V_o \end{aligned} \quad (31)$$

Fig. 12 depicts the second phase $[0, (1-D) T]$, during which BJT2 is off and BJT1 is on. The following are the possible resulting equations for this phase:

$$\begin{aligned} v_{L1} &= L_1 \frac{di_1}{dt} = V_s \\ v_{L2} &= L_2 \frac{di_2}{dt} = -v_{Cs} - v_{Cm} \\ v_{L3} &= L_3 \frac{di_3}{dt} = -V_o \end{aligned} \quad (32)$$

Fig. 14 depicts the third phase $[0, (1-D) T]$, during which BJT1 is off and BJT2 is on. The equations that emerge to describe this period are:

$$\begin{aligned} v_{L1} &= L_1 \frac{di_1}{dt} = V_s - v_{Cm} \\ v_{L2} &= L_2 \frac{di_2}{dt} = -v_{Cs} = v_{C1} - v_{Cm} \\ v_{L3} &= L_3 \frac{di_3}{dt} = v_{C1} - V_o \end{aligned} \quad (33)$$

According to the volt-second area theory, the average voltages across the inductors have zero values, which means:

$$\begin{aligned} V_{L1} &= V_s - (1 - D) V_{Cm} \\ V_{L2} &= -DV_{Cs} + (1 - D)V_{C1} - V_{Cm} \\ V_{L3} &= D V_{C1} - V_o \end{aligned} \quad (34)$$

The conversion ratio voltage can be gained as follows:

$$\begin{aligned} V_{Cm} &= \frac{1}{1-D} V_s \\ V_{Cs} &= -DV_{Cm} = \frac{-D}{1-D} V_s \\ V_{C1} &= \frac{V_o}{D} \end{aligned} \quad (35)$$

Thus:

$$V_o = \frac{D(1+D)}{(1-D)} V_s \quad (36)$$

According to Equation (36), the bucking regime for $0 < D < -1 + \sqrt{2}$ in DSSB is operated in it to waive the load voltage, V_o , regarding the supply voltage, V_s . The DSSB is used to raise the load voltage, V_o , with an estimate to the supply voltage, V_s , while the converter is operating in the region of the improved regime for $-1 + \sqrt{2} < D < 1$.

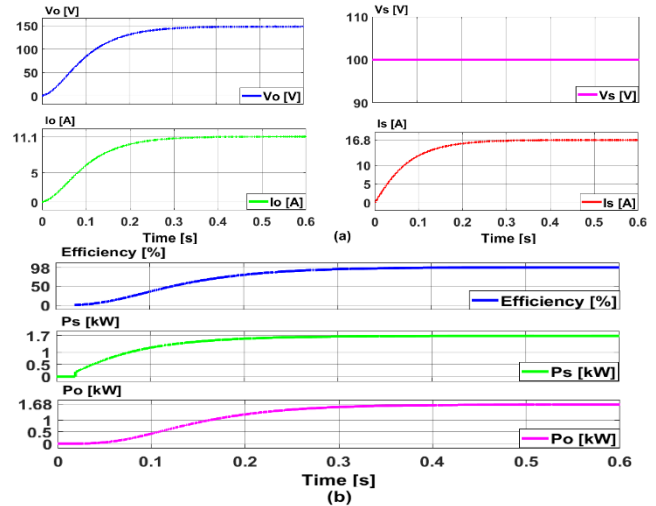


Fig. 17. DSSB Matlab simulation results: (a) represent the output and input voltages and currents, (b) represent the output and input powers with the converter efficiency of 98%

The voltage/current waveforms, power, and proposed DSSB converter efficiency simulation for $D = 0.45$ are shown in Fig. 17; they were developed in Matlab/Simulink, and the target switching frequency of the DSSB is $f = 4 \text{ kHz}$. The results show the efficiency of the proposed converter ranging from 96%–98% in terms of low rise time, 0.3 s, and settling time of 0.4 s.

4.3 Control Strategy of DSSB Converter

To improve the efficiency of the converter and lower the total harmonic content in its input-output voltages and currents, a proposed voltage current controller for a DSSB converter provides an example of a load voltage current regulation-based power factor correction method.

The operating point of interest is utilized as a small-signal technique as a linear time-invariant system with a certain switching cycle of the switches to simulate the behavior of the converter. The DSSB representation using open-loop and closed-loop transfer functions enables this small-signal principle (Ayachit et al., 2016; Kanimozhi et al., 2017; Corti et al., 2023).

The open-loop and closed-loop transfer functions of the DSSB simulation model were computed once its frequency response was determined. Then, a suitable compensator is created and compared to the linear model. The controller gain

was adjusted so that the DSSB is operated within the intended operating range by repeating the small-signal technique for various operating points, such as various switching ratios (duty cycle) or desired output voltage levels.

By using algorithm form, the small signal model was established and verified as follows (Hart, 2010; da Rocha Carvalho and Toffoli, 2017; Emar, 2024):

- For the DSSB small-signal analysis, various disorder input voltages and currents were chosen.
- Using methods like interactive modeling of a loop with a root locus and Bode graphs or PI autotuning, the resulting linear model compensator was created and tuned.
- Creating a compensator with a gain schedule to regulate the power electronics device under all possible operating circumstances.
- To manage the DSSB converter across the whole range of operating circumstances, a planned gain compensator was created.
- By simulating the controller design against a nonlinear model of a power electronics system, you may verify and test it.
- By simulating the controller design against a nonlinear model of the DSSB, it was validated and put to the test.
- For the implementation of a control system and an appropriate prototyping model, MATLAB and Simpler 7 models were created automatically.

Two loops are needed for the voltage/current control: an internal source current loop and an external source voltage loop. To create the duty cycle using the appropriate PWM with two ramp signals phase shifted with 180° in order, it is necessary to obtain the requisite load current and load output voltage with a very low ripple. To create the required output power with a value equivalent to the permitted possible normalized input power, the inductor currents and voltage are measured and adjusted (Emar, 2016; Emar et al., 2020).

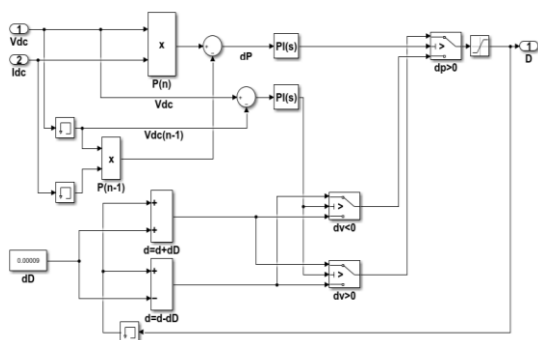


Fig. 18. The control scheme for producing the DSSB switching ratio D

The converter output quantities consist of averaged DC (source voltages and currents) and low-frequency AC. according to the algorithmic approach described above: First, for each switching cycle, $T = 1/f$, the average values of their current and prior instantaneous values are computed as follows:

$$X(n) = \frac{1}{T} \int_{nT}^{(n+1)T} xdt \quad (37)$$

$$X(n-1) = \frac{1}{T} \int_{(n-1)T}^{nT} xdt$$

Second, the average current and previous values of the relevant load currents and voltages are multiplied to determine the value of the current and prior load power.

Consequently, disruptions at a frequency lower than the converter switching frequency may occur for the duty cycle D, the dc load voltage, current, and mutual product. All other conversion variables will therefore oscillate at this frequency around their respective dc values. Therefore, the switching method illustrated in Fig. 18 is used to calculate the averaged load voltages, currents, and duty cycle. The control algorithm of this DSSB operates by continuously observing the rate at which power fluctuates in response to changes in load voltage and current. The DC-DC DSSB converter's goal is to provide the least amount of load current and voltage ripple possible while maximizing power transfer efficiency. The converter PWM signal generator receives the output of this controller after which a duty ratio of $D \leq 1$ is generated.

4.4 Bode Plots of DSSB Converter

One feature is that the system frequency response is utilized to assess the stability of the system. Gain margin and phase margin can be utilized in this situation to show the system margins before becoming stable or unstable (Hart, 2010).

The Bode diagrams for the DSSB converter open-loop and closed-loop frequencies with the aforementioned load and a converter switching frequency of 4 kHz are created in the Simpler environment and displayed in Figs. 19 and 20. Additionally, the open-loop frequency responses of the proposed converter are performed to investigate its dynamic performance and to display the range of the bandwidth, the obvious resonances, the system stability, or how far the system is from an unstable condition in terms of phase and gain. It is also done to detect the resonance in the system and the necessary filters, or controllers' parameters. Fig. 19 displays the Bode plots of the DSSB open-loop current gain transfer function $G_i(s) = I_o / I_s$ and voltage gain $G_v(s) = V_o / V_s$. The open-loop voltage gain (transfer function) is given as:

$$G_v(s) = k_{pv} * G_a(s) = 12.5 * \frac{8e-6}{(1 + 0.02s)^3} \quad (38)$$

And the open-loop current gain transfer function is expressed as follows:

$$G_i(s) = k_{pi} * G_b(s) = 25 * \frac{1e-4}{s(1 + 0.01s)^2} \quad (39)$$

The closed loop phase margin is the extra phase delay required to bring the open loop phase to -180° at the frequency where the open loop amplitude is 0 dB.

According to the Bode plots of the closed-loop system in Fig. 20 and as displayed in MATLAB/Simulink Simplorer 7, the closed-loop block diagram with two PI controllers is stable since the zero crossing from 0 dB to a phase angle less than 180° or 55° , occurs. Additionally, the gain margin during the 180° transition is approximately 82 dB higher than zero.

According to the control loop output voltage design, the function frequency is roughly 23 kHz, the current gain is about 700 Hz, and the closed loop voltage gain transfer function bandwidth is 355 Hz. For frequencies below 1 MHz, the gain attenuation factor (slope) is -40 dB/decade, or a factor of -24 dB/octave. The current gain transfer function indicates that the converter can display the properties of an undamped system in the current loop diagram, with one pole at the origin and two negative real poles (Wu et al., 2018; Osmani et al., 2021; Masmoudi et al., 2022; Nizami et al., 2022).

5. CONTROL STRATEGY OF PMSG-BASED WIND ENERGY CONVERSION INVERTER SYSTEM

The main target of this control is to generate the duty cycle of DSSB and gating signals for a VSI to extract optimum power from the WT.

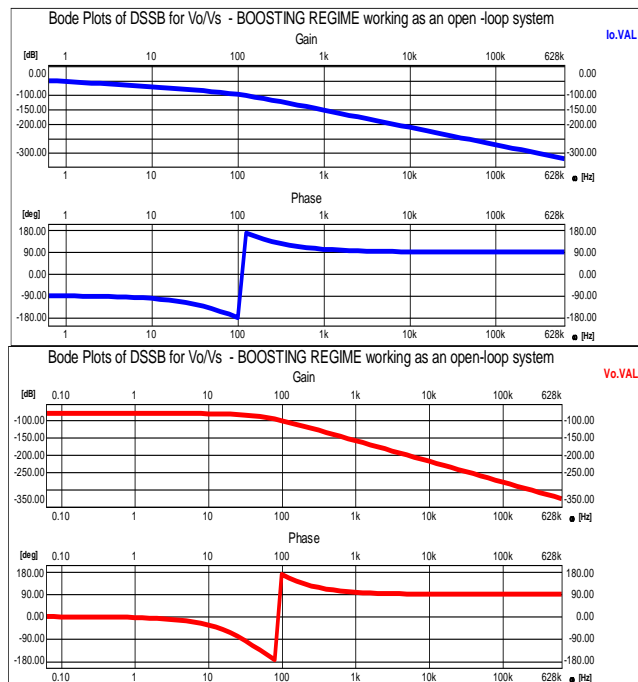


Fig. 19. Bode graphs of DSSB, a closed-loop system, showing the voltage gain V_o/V_s and the current gain I_o/I_s during the boosting regime

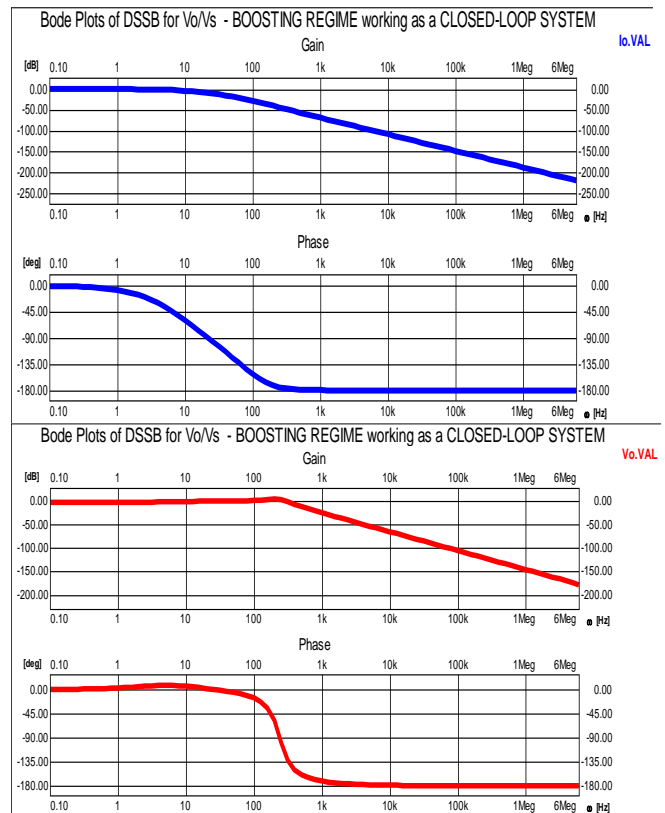


Fig. 20. Bode graphs for the closed-loop DSSB control system, displaying the current gain I_o/I_s and voltage gain V_o/V_s during the boosting phase

5.1 Block Diagram of the PMSG with the DSSB and VSI

The proposed structure of the PMSG control strategy using DSSB and VSI is shown in Fig. 21. The control strategy includes the following steps:

- Estimate the turbine reference speed ω_{ref} using the OPPT technique.
- The output power, speed, and torque of PMSG can be estimated through Equations (13) and (14) in addition to the parameters of PMSG used in this paper from Table 1.
- The reference power of PMSG is determined from Equation (24) as a function of the rotor reference speed.
- The system's actual speed is compared with its reference speed generated by OPPT to produce the reference q-component of the stator current i_{qsref} .
- The comparative result between the reference and the actual dq components of the stator currents is then used to control the generator stator currents i_{ds} and i_{qs} as shown in Fig. 6. These two current components are important to control the generator output power and torque.
- Trigger signals for VSI are generated as shown in Fig. 21 below. The purpose of this command is to cyclically control the two DSSBs, BJT1, and BJT2 shown in Fig. 1, to obtain the maximum optimal performance from the available wind energy.

The control algorithm of Fig. 22 includes the use of two PI controllers for the dq components of stator PMSG currents. This is a well-proposed field-oriented control solution for electric machines. This solution usually guarantees better performance than, for example, non-linear sliding mode control that is demonstrated in some references, but at a certain cost of robustness.

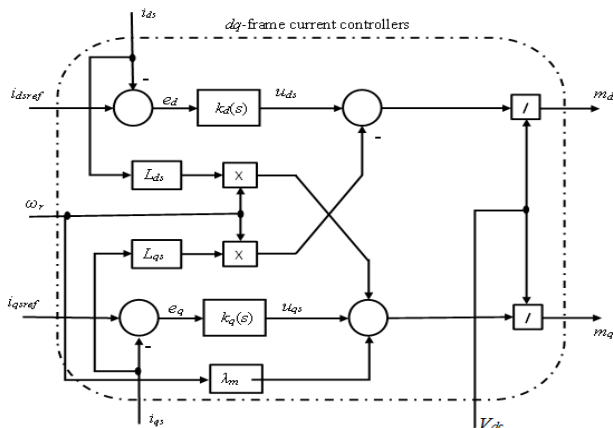


Fig. 21. Generation of the control signals for the VSI

5.2 PI-controllers' Parameters and Transfer Function Determination

For a PMSG machine with non-salient poles, the machine inductive parameters are $L_q = L_d = L_s$. Thus, the transfer function parameter of the two PI controllers becomes:

$$k_d(s) = k_q(s) = \frac{sL_s + R_s}{s\tau_i} = k_p + \frac{k_i}{s} \quad (40)$$

By closed-loop, the existing controllers' transfer function is:

$$G_s(s) = \frac{\omega_c}{s + \omega_c} \quad (41)$$

The two PI parameters are chosen to eliminate the generator stator circuit time constant as follows:

$$\begin{aligned} k_p &= L_s \omega_c \\ k_i &= R_s \omega_c \end{aligned} \quad (42)$$

Thus, the bandwidth of the current loop is set to be: $f_c = \omega_c / 2\pi = 2000 \text{ Hz}$, which is 1/2 of the DSSB' chosen switching frequency $f_s = 4 \text{ kHz}$.

The open-loop transfer function of the speed controller is:

$$G_s(s) = (k_{pw} + \frac{k_{iw}}{s}) \frac{\omega_c}{s + \omega_c} \frac{1}{Js+B} = \frac{\omega_s}{s + \omega_s} \quad (43)$$

The crossover frequency, ω_s in Equation (43) is chosen to be much smaller than the control current loop bandwidth, ω_c , so that $|\frac{\omega_c}{s + \omega_c} \frac{1}{Js+B}| \approx 1$. The speed controller parameters are given as follows:

$$\begin{aligned} k_{pw} &= J \omega_s \\ k_{iw} &= k_{pw} \omega_{co} \end{aligned} \quad (44)$$

Where ω_{co} is the corner frequency of the PI speed controller and that is selected to give a phase margin of $PM = 75^\circ$ to obtain a fast dynamic response.

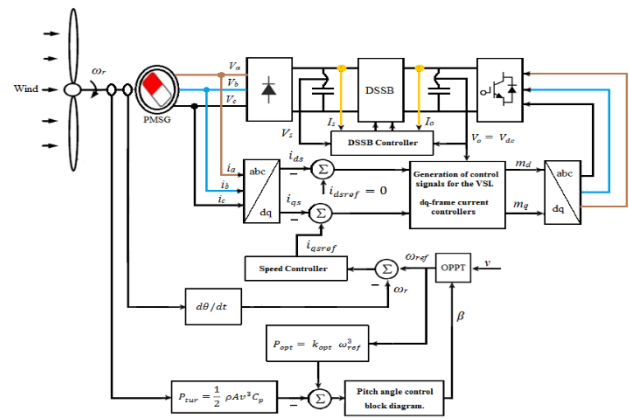


Fig. 22. PMSG-based WT control block diagram

6. SIMULATION AND EXPERIMENTAL RESULTS

In this research, a small signal deviation for the active switches with two PI controllers is used to select the MPPT method of the PMSG.

Comparing the proposed modified DSSB converter processor to existing SEPIC converter topologies reported by (Wu et al., 2018; Jiang et al., 2020; Osmani et al., 2021; Masmoudi et al., 2022; Nizami et al., 2022) the normalized voltage gain is greatly increased. Since the duty cycle is a modifiable parameter, the converter operating theory suggests that the amount of lowering the inductor current ripple should also be modifiable.

6.1 Voltage Gain of the Proposed DSSB in Comparison to Other SEPIC Converter Topologies

The suggested DSSB's simulation parameters converter are shown in Table 2. In light of the previously described analysis, the salient features of Table 3 are utilized to emphasize the technical and preference advantages of DSSB in relation to alternative SEPIC converter topologies, namely standard and modified multiplier SEPICs. The duty ratio is a changeable parameter that suggests that the degree of inductor current ripple reduction should also be adjustable, based on the requirements of the converter principle of operation.

As can be seen in Fig. 23, the normalized voltage gain with the revised DSSB conversion processor is significantly superior than previous SEPIC topologies indicated in Table

3. The conversion ratio $D = 0$ produced the lowest value of this ripple, whereas $D = 1$ theoretically produced the highest. Furthermore, the maximum ripple percentage of the output voltage content sharply rises as the duty cycle, D , approaches unity.

Moreover, the results generated above in this paper show that the DSSB efficiency (the ratio of output power to input power) is in the range of 95%–98%. This result is comparable to that of the BB converter, which has been documented in numerous scientific studies and is preferred over many other DC-DC converters. However, in terms of power capacity and voltage/current ratings, DSSB beats all other comparable DC-DC converters considered in this paper.

Furthermore, employing PWM modulation approaches,

inverting buck-boost (BB), SEPIC, and DSSB converters are compared. Thus, the proposed converter DSSB outperforms the BB converter in terms of efficiency, harmonic content generated in the converter current, and voltage waveform (Yazdani, 2010; Emar et al., 2011; Azzaoui et al., 2017; Emar et al., 2024).

6.2 WECS with Only DSSB and Resistive Load

A simulation model of the proposed system is created in Simulink/Matlab to study performance improvements using results from the analytical and simulation study performed above. The test is done first for the PMSG driven by a WT and supplying a DC resistive load via a DSSB. To validate the theoretical analysis and simulation, the DSSB transformer working in the CCM was designed and

Table 2. Design specifications of DSSB

Parameter	Symbol	Real value	Type
Input voltage	V_s	100 V	DC power source
Input inductor	L_1	50 mH	Core NEE-65/33 by Thornton, $N_{L1} = 180$ turns – $4 \times$ AWG 27
Rated input power	P_{in}	250 W	-
Rated output power	P_o	245 W	-
Input inductor current ripple	Δi_{L1}	0.12 A	-
Output inductor current ripple	Δi_{L3}	0.08 A	-
Shunt inductor	L_2	20 mH	Core NEE-65/33 by Thornton, $N_{L2} = 180$ turns – $4 \times$ AWG 27
Output inductor	L_3	670 μ H	core NEE-65/33 by Thornton, $N_{L3} = 45$ turns – $5 \times$ AWG 24
Smoothing capacitor	C_1	470 μ F	Electrolytic capacitor by Hitano
Shunt capacitor	C_2	4.7 μ F	Nichicon's electrolytic capacitor
Shunt capacitor	C_3	4.7 μ F	Nichicon's electrolytic capacitor
Output capacitor	C_4	470 μ F	Hitano's electrolytic capacitor
Switching ratio	D	0.4	-
Output voltage	V_s	50 V	-
Load resistance	R	10 Ω	Ceramic resistor by LW
Switching frequency	F	4 kHz	Signal generator

Table 3. DSSB comparison to traditional, and multiplier SEPICs

Performance	Type of sepic		
	Traditional sepic as explained in Emar et al. (2024)	Modified multiplier (Emar et al., 2024)	DSSB Fig. 1
Normalized voltage gain	$V_o = \frac{D}{1-D} V_s$	$V_o = \frac{D^2}{1-D} V_s$	$V_o = \frac{D(1+D)}{1-D} V_s$
Example: $V_s = 50$ V	$D = \frac{1}{4} \Rightarrow V_o = \frac{V_s}{3} = 6.6$ V $D = \frac{1}{2} \Rightarrow V_o = V_s = 50$ V $D = \frac{3}{4} \Rightarrow V_o = 3V_s = 150$ V This SEPIC topology is an up/down converter when D is less than or greater than 0.5, respectively.	$D = \frac{1}{4} \Rightarrow V_o = 4.16$ V $D = \frac{1}{2} \Rightarrow V_o = 25$ V $D = \frac{3}{4} \Rightarrow V_o = 112.5$ V This SEPIC topology is an up/down converter if D is less than or greater than 0.618, respectively.	$D = \frac{1}{4} \Rightarrow V_o = 20.8$ V $D = \frac{1}{2} \Rightarrow V_o = 75$ V $D = \frac{3}{4} \Rightarrow V_o = 262.5$ V When D is less than or more than 0.414, this SEPIC topology functions as an up/down converter and has a substantially higher step-up voltage than other topologies.
Normalized ripple in the inductor supplies current	$\Delta i_L = \frac{V_s}{fL} D$ for all values of duty ratio D.	$\Delta i_L = \frac{V_s}{fL} D$ for all values of duty ratio D.	$\Delta i_L = \frac{V_s}{fL} D$ for all values of duty ratio D.
Number of capacitors and power electronic devices	Two capacitors, two inductors, one diode, and one transistor	One transistor, three diodes, three capacitors, and three inductors	Two transistors, three diodes, four capacitors, and three inductors

rigorously tested according to the specification parameters listed in Table 2. The physical parameters of WTs are shown in Table 4 and those of PMSG are shown in Table 5.

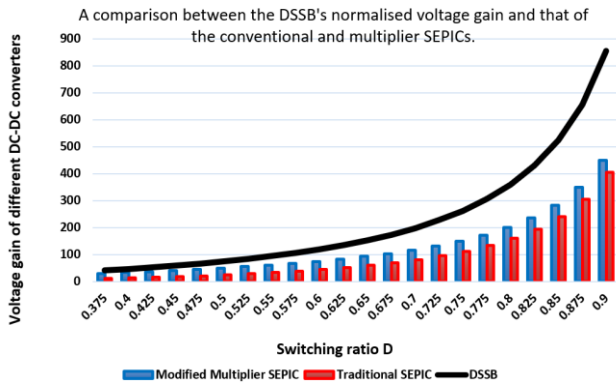


Fig. 23. A graph comparing the DSSB's normalized voltage gain to several alternative SEPIC topologies

Table 4. Wind turbine parameters

Parameter	Symbol	Real value	Unit
Nominal mechanical power	P_{m-turb}	12.3E3	W
Nominal wind speed	V_{base}	12	m/s

Simulation of Figs. 24 and 25 are carried out to show the dynamic performance of the proposed WECS with the DSSB converter and only a resistive load of $R = 13.3 \Omega$. Fig. 24 shows plots of the WECS variables and the DSSB-controlled output voltage and current for the wind speed variation profile using only the AC small signal technique. One can see from Figs. 24 and 25 the fast dynamic response of the DSSB to the disturbance observer by eliminating the parasitic effect of the DSSB capacitive and inductive parameters and reduced peak-to-peak ripple in the DSSB output current and voltage. The simulation seemed to be done for a duty ratio, of $D = 0.46$, which means that $V_s < V_o$.

In the OPPT zone, the DSSB's descending mode output voltage and current are displayed for a step change in wind speed. The DSSB-controlled output voltage and current (V_o

and I_o) precisely follow the required input voltage and current (V_s and I_s) in behavior based on the change in wind speed. However, the output voltage is lower than the input voltage according to the relationship $V_o = \frac{D(1+D)}{1-D} V_s$ and at the same time, the output current is higher than the input current in the inverse relationship $I_s = \frac{D(1+D)}{1-D} I_o$, which means that the DSSB works in the bucking regime. Furthermore, there is an overshoot of voltages and currents due to the parasitic effects of the capacitive inductive parameters of the DSSB and the inductive generation of reactive power by the PMSG.

From Fig. 24, it can be observed that the output power of the DSSB, P_{out} , has almost an exact value as its input power, P_{in} , and changes based on the wind speed profile. Thus, the DSSB efficiency under the given WECS operating conditions is almost 96%.

Fig. 25 shows the PMSG voltage and current responses in various timing simulations for the DCSB output voltage mode control conditions. First, it simulates a 5-second wind speed shift from 12 m/s to 16 m/s and displays the output voltage and current behavior of the PMSG. Lastly, it displays once more how the output voltage and PMSG current react to a slow decrease in wind speed from 16 to 14 m/s throughout the 8-second simulation.

In conclusion, because the DSSB is effectively a boost converter followed by a buck converter, it operates similarly to a conventional buck-boost converter. A non-inverted output, or one with the same voltage polarity as the input, and the addition of extra capacitive and inductive filters to couple energy from the input to the output are two of its main differences, though. It can also conduct genuine shutdown, which means that after a very large transient discharge of charge, the output decreases to 0 V when the switch is switched off.

By contrasting the suggested WECS scheme with a DC chopper-regulated WECS (Ali et al., 2013; Muniyandi et al., 2019; Guesmi et al., 2021) it is possible to successfully control the DC-link voltage and maintain the voltage stress of the DSSB switches below the safety limit. Furthermore, the converter's capacity is decreased and its operating duration is shortened, which lessens the load's ability to dissipate heat.

Table 5. PMSG specification parameters

Parameter	Symbol	Real value	Unit
Nominal power of PMSG	P_{gbase}	12.3E3/ 0.9	W
Maximum power at base wind speed (p.u. of nominal mechanical power)	P_{pu}	0.85	-
Base rotational speed (p.u. of base generator speed)	n_{pu}	1.2	p.u.
Stator phase resistance R_s (Ohm)	R_s	0.0485	Ω
Stator inductances	[$L_d(H)$, $L_q(H)$]	[0.395E-3, 0.395E-3]	H
Flux linkage	Ψ	0.1194	Web
Inertia, viscous damping, pole pairs, static friction	[J (kg·m ²), F (N·m·s), $p(2)$, T_f (N·m)]	[0.0027, 0.0004924, 4, 0]	
Initial conditions	[ω_m (rad/s) theta (deg) i_a , i_b (A)]	[0, 0, 0, 0]	
Rotor flux position when theta = 0	90° behind phase A axis		

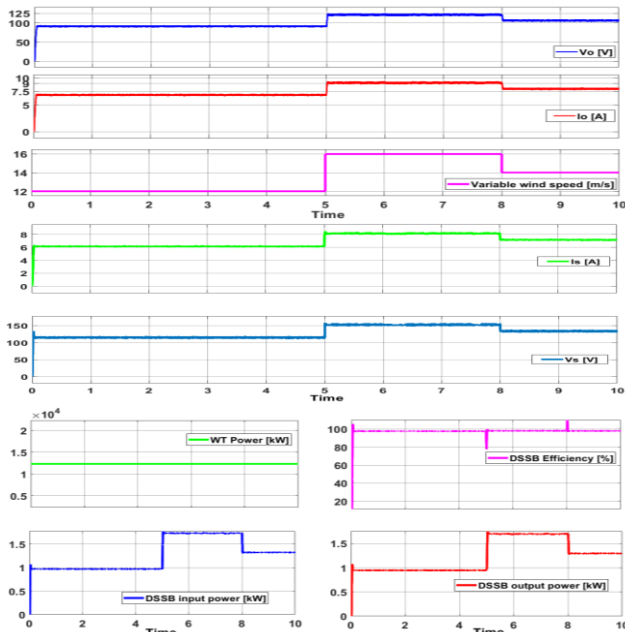


Fig. 24. Plots of the DSSB variables for a step-change of wind speed with a resistive load only

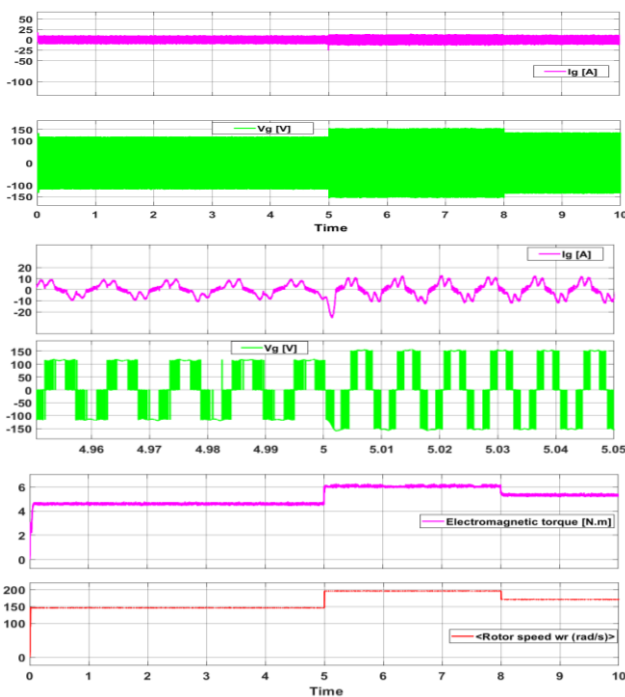


Fig. 25. Plots of the PMSG variables for a step-change of wind speed with a resistive load only

Consequently, the DSSB control block diagram, rather than the PMSG controller, which independently controls the PMSG current to be injected and the corresponding active and reactive power to the load in accordance with the OPPT control mode, is responsible for controlling the DC link voltage on the PMSG side using the proposed small-signal AC analysis previously mentioned. Since the two systems

have different dynamics and time constants, this improves the system's capacity to decouple the PMSG output voltage and current regulation from the DSSB's DC output circuitry. Consequently, as wind speed changes, DSSB input voltage and current V_o and I_o also change.

Fig. 25 also shows that the PMSG shaft speed and developed torque waveforms have the same shape as the wind speed profile. Also, it shows that the electromagnetic torque generated by the PMSG almost follows the torque generated by the WT. The angular speed profile does not exceed the optimum value and does not have an overshoot. However, a quick speed response requires rapid changes in the generator torque. However, the WT torque is more affected by the change in wind speed than the torque produced by the PMSG.

6.3 WECS with DSSB, VSI, and Resistive Inductive Load ($R = 20 \Omega, L = 10 \text{ mH}$)

Fig. 26 shows plots of the DSSB variables for the wind speed variation profile in the OPPT region using a small AC signal technique. The simulation seemed to be done for a duty ratio, of $D = 0.2$, which means that $V_s > V_o$. Compared to other possible topologies in the literature, the proposed properties of DSSB with VSI topology show that the control of the voltage source by the inverter works well for variations in wind speed and a given load profile.

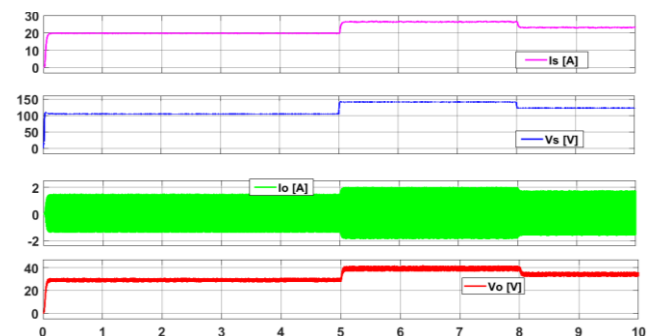


Fig. 26. DSSB current and voltage waveforms in response to a step change in wind speed with a resistive inductive load

The size of the simulation step was set to 10 s, but the observer and control sample time and controllers were updated every $20E-6$, with a typical PWM 4 kHz control cycle in practical applications. In real-time implementations, the wind speed estimate and the rotor speed management updates may be much longer.

The PMSG speed and torque, as well as the stator voltage and current waveforms of the PMSG, are shown in Figs. 27 and 28, respectively. The simulation parameters waveforms for the proposed VSI are listed in Table 5.

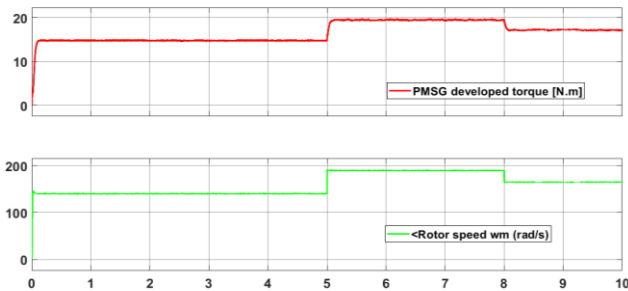


Fig. 27. PMSG shaft speed and generated torque waveforms in response to a step change in wind speed with a resistive inductive load

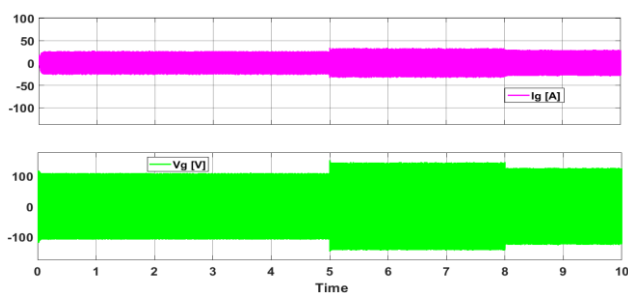


Fig. 28. PMSG stator current and voltage waveforms in response to a step change in wind speed with a resistive inductive load

In conclusion, Muniyandi and Rajagopal (2019) looked into the use of a zero-voltage resonant switch converter in the development of a permanent magnet synchronous motor drive that is fed by a dynamic solar array and operates independently. It is recommended to utilize a permanent magnet synchronous motor (PMSM) drive with an SPV array fed Zero Voltage Switching (DISOZVS) resonant converter in order to improve the suggested WECS's efficiency and reduce vibration across the load. The ZVS converter is a buck-boost circuit that operates as a boost circuit when discharging and as a buck circuit while charging.

In contrast to the research conducted by Muniyandi and Rajagopal (2019), the WECS-based DSSB converter proposed in this paper has higher efficiency and voltage gain, is less complex, and is less expensive. This is because the Muniyandi and Rajagopal research uses a Dual-input-Single Output ZVS converter, which may make it more difficult to achieve the goal of high-efficiency power conversion and ultimately increase its cost.

A more effective approach with fewer, smaller external components is provided by the proposed DSSB converter. With these few components, it is capable of stepping up or down voltages with the same sign as the input voltage. Additionally, it provides greater efficiency over a broad range of input and output voltages together with a lower operating duty cycle. Furthermore, the DSSB converter is far less expensive than many other converters.

Additionally, in 2013, Ali et al. looked into thorough models of WTs to examine power and voltage variations of PMSG. The voltage fluctuation emitted is evaluated using the short-time flicker index. To lessen flicker emissions, a voltage regulation loop supports the grid-side converter's control scheme. This paper evaluates the voltage fluctuation emission using the small AC signal deviation with PI controllers. PI controllers are used in the control structures created in this work because they perform well in controlling DC variables.

According to Ali et al. (2013), while employing MPPT, the wind speed sensor is not used; as a result, the generator speed is controlled by generator torque control. Furthermore, as stated by Ali et al. (2013), the rotor inertia keeps the rotor speed constant. Because the generator's torque is based on the rotor speed, the electromagnetic torque is somewhat delayed.

However, in this work, optimality is attained when pitch angle control and speed sensor measurement are used to regulate the generator speed such that it follows the optimal power curve. One potential solution to the issue of system parameter change is to combine small AC signal analysis with PI controllers rather than traditional PI controllers. Thus, it is possible to attain a good control performance. Consequently, this paper proposes the application of PI controllers and AC small signal analysis to the PMSG converter controller system.

7. CONCLUSIONS

The paper presents a control strategy for an autonomous variable speed wind system driving a PMSG using a newly developed DSSB converter and a VSI, along with extensive analysis and simulation using MATLAB/SIMULINK. Although the control techniques presented are well known and have already been used in research and control applications, the contribution of this work is the following:

- The research shows a new modified DC-DC converter topology known as the DSSB. This topology can be used in a step-up application (increase mode) and/or in a step-down application (bucking mode).
- The main principle of so-called optimal power monitoring (OPPT) by optimizing energy extraction from the Wind Energy conversion system (WECS) using a proposed DSSB converter as a wind-based wind-based PMSG.
- A closed-loop voltage versus current mode controlled DSSB with a two dual-lead PI controller is a method that is used to optimize the dynamic behavior of the proposed converter.
- The frequency response and transfer functions of the DSSB simulation model are used to illustrate its dynamic behavior using a small-signal method.
- Pitch angle control and speed sensor measurement combined with generator power tracking the optimal power curve result in the optimal operation of the proposed system which is another advantage of this paper.

- Combining small AC signal analysis with PI controllers, as opposed to using only traditional PI controllers as in many other research studies, is one possible way to address the problem of system parameter change.
- Moreover, a comparative study between the proposed converter and the currently known buck-boost converter has been presented. In addition, a comparison of the suggested converter's complexity, mean value, rectified mean value, RMS value, crest factor, ripple factor, harmonic factor, and harmonic content distortion has been made with other comparable topologies of the SEPIC converter. The proposed converter DSSB is the most suitable due to its excellent input/output response capacity, harmonics reduction, and low ripple content, the DC-DC converter provides practically the rated efficiency output, a closed power factor, without waveform ripple additionally, and overall outstanding stability.
- Verification of simulation and presentation of very good control dynamic quality of the proposed WECS with the DSSB converter and VSI in the form of responses to wind profile with step is presented.

The simulation results have been implemented by the AC small signal algorithm for the DSSB and PMSG-based WT control block diagram shown in Fig. 22, using the power control, with a wind speed variation profile energy to show the DSSB and PMSG dynamic behavior and extraction of maximum power from the available wind energy.

Finally, it explains how to check the voltage source of the inverter using the voltage control strategy to ensure the required stress voltage in terms of size and frequency for a disgusting induction load. The simulation results demonstrated that, despite the wind speed profile's fluctuation, the control strategy's effectiveness is adequate.

REFERENCES

- Adhul, S.V., Ananthan, T. 2020. FOPID controller for the buck converter. *Procedia Computer Science*, 171, 576–582.
- Ayachit, A., Reatti, A., Kazimierczuk, M.K. 2016. Small-signal modeling of PWM dual-SEPIC DC-DC converter by circuit averaging technique. In *IECON 2016-42nd Annual Conference of the IEEE Industrial Electronics Society, IEEE*, 3606–3611.
- Azzaoui, M.E., Mahmoudi, H. 2017. Fuzzy-PI control of a doubly fed induction generator-based wind power system. *International Journal of Automation and Control*, 11(1), 54–66.
- Boufadene, M., Belkheiri, M., Rabhi, A. 2018. Adaptive nonlinear observer augmented by radial basis neural network for a nonlinear sensorless control of an induction machine. *International Journal of Automation and Control*, 12, 27–43.
- Corti, F., Laudani, A., Lozito, G.M., Reatti, A., Bartolini, A., Ciani, L., Kazimierczuk, M.K. 2023. Modelling of a pulse-skipping modulated DC-DC buck converter. *IET Power Electronics*, 16, 243–254.
- da Rocha Carvalho, J.A., Tofoli, F.L. 2017. Small-signal model validation of a SEPIC converter based on the three-state switching cell in CCM using the PWM switch model. In *2017 Brazilian Power Electronics Conference (COBEP), IEEE*, 1–6.
- El-Hasan, T. S., Luk, P. C. K., Bhinder, F. S., Ebaid, M. S. 2000. Modular design of high-speed permanent-magnet axial-flux generators. *IEEE Transactions on Magnetics*, 36(5), 3558–3561.
- Emar, W. 2024. Hysteresis current-mode regulated modified sepic-buck converter used for solar photovoltaic systems. *Arabian Journal for Science and Engineering*. 49, <https://doi.org/10.1007/s13369-023-08660-5>.
- Emar, W., Haitham I., Hasan K., Osama F. Hani A. 2024. A new double-switch sepic-buck topology for renewable energy applications. *Energies* 17(1), 238.
- Emar, W., Huneiti, Z., Al-Omari, Z. 2020. Induction motor current ripple minimization with PV-based SEPIC-cascaded inverter. *International Journal of Modelling, Identification and Control*, 35, 151–165.
- Emar, W., Maher, R.A., Jalil, A. 2011. Constant frequency digital hysteresis-band current controller for a three-phase voltage inverter. *Control and Intelligent Systems*, 39, 108.
- Emar, W., Saraereh, O.A. 2019. Analytical and comparative study of different types of two-leg chopping-up regulator. *International Journal of Advanced Computer Science and Applications*, 10, 5.
- Gajewski, P., Pieńkowski, K. 2016. Advanced control of direct-driven PMSG generator in wind turbine system. *Archives of Electrical Engineering*, 65, 643–656.
- Guesmi, S., Jamoussi, K., Chrifi-Alaoui, L., Ghariani, M., Baazouzi, K. 2021. Passivity based control PBC applied in the buck converter of the stand-alone photovoltaic system. *International Journal of Automation and Smart Technology*, 11, 2127.
- Hart, D.W. 2010. Chapter 8-inverters. *Power Electronics*. Ed. by Darlene M. Schueller. McGraw-Hill, 357–358.
- Jiang, L., Li, Y., Huang, Y., Yu, J., Qiao, X., Wang, Y., Huang, C., Cao, Y. 2020. Optimization of multi-stage constant current charging pattern based on Taguchi method for Li-Ion battery. *Applied Energy*, 259, 114148.
- Kanimozhi, G., Meenakshi, J., Sreedevi, V.T. 2017. Small signal modeling of a DC-DC type double boost converter integrated with SEPIC converter using state space averaging approach. *Energy Procedia*, 117, 835–846.
- Kasem Alaboudy, Ali H., Daoud, Ahmed A., Desouky, Sobhy S., Salem, Ahmed A. 2013. Converter controls and flicker study of PMSG-based grid connected wind turbines, *Ain Shams Engineering Journal*, 4(1), 75–91.
- Magossi, R.F., Han, S., Machado, R.Q., Oliveira, V.A., Bhattacharyya, S.P. 2020. Geometric-based PID control design with selective harmonic mitigation for DC-DC converters by imposing a norm bound on the sensitivity function. *IET Control Theory & Applications*, 14, 3330–3337.

- Masmoudi, A., Abdelkafi, A., Krichen, L., Saidi, A.S. 2022. An experimental approach for improving stability in DC bus voltage of a stand-alone photovoltaic generator. *Energy*, 257, 124797.
- Mostaan, A., Gorji, S.A., Soltani, M.N., Ektesabi, M. 2017. A novel single switch transformerless quadratic DC/DC buck-boost converter. In 2017 19th European Conference on Power Electronics and Applications (EPE'17 ECCE Europe), IEEE, P-1.
- Muniyandi, C., Rajagopal, S.K. 2019. Implementation of standalone dynamic solar array fed permanent magnet synchronous motor drive using zero voltage switching resonant converter for the reduction of switching losses and oscillations. *Journal of Vibroengineering*, 21, 1483–1509.
- Nizami, T.K., Gangula, S.D., Reddy, R., Dhiman, H.S. 2022. Legendre neural network based intelligent control of DC-DC step down converter-PMDC motor combination. *IFAC-PapersOnLine*, 55, 162–167.
- Osmani, K., Haddad, A., Lemeland, T., Castanier, B., Ramadan, M. 2021. An investigation on maximum power extraction algorithms from PV systems with corresponding DC-DC converters. *Energy*, 224, 120092.
- Raj, T.A.B., Ramesh, R., Maglin, J.R., Vaigundamoorthi, M., Christopher, I. W., Gopinath, C., Yaashuwanth, C. 2014. Grid connected solar PV system with SEPIC converter compared with parallel boost converter based MPPT. *International Journal of Photoenergy*. 2014, 385720.
- Wu, H., Han, M., Sun, K. 2018. Dual-voltage-rectifier-based single-phase AC–DC converters with dual DC bus and voltage-sigma architecture for variable DC output applications. *IEEE Transactions on Power Electronics*, 34, 4208–4222.
- Yazdani, A., Iravani, R. 2010. Voltage-sourced converters in power systems: Modeling, control, and applications. John Wiley & Sons.